

# Height Estimation and Image Tracking Control of an Indoor Quad-Rotor Craft via Multi-Vision Systems

<sup>1</sup>Juhng-Perng Su and <sup>2</sup>Kuo-Hsien Hsia

## Abstract

This paper presents a novel height estimation and image tracking control scheme for an indoor quad-rotor craft based on image servoing techniques. Two multi-vision systems, namely, stereo vision system and humanoid vision system, respectively, were proposed for use as image servoing subsystems whose performances were examined and compared. A specific landmark was used as a target for image tracking by which the height and position of a quad-rotor craft were estimated for positioning control. The experimental results suggest that the performance of HSV color model based tracking method either by stereo vision system or humanoid vision system is quite acceptable. Specifically, the accuracy of the humanoid vision system seems a bit better than the stereo vision system for quad-rotor craft height estimation.

**Keywords:** height estimation, quad-rotor craft, image servoing, stereo vision, humanoid vision.

## 1. Introduction

From the application point of view, autonomous unmanned rotorcrafts obviously prevail over the fixed-wing aircrafts because they are capable of taking off and landing vertically as well as hovering in the air. They can be found in numerous applications including taking aerial photograph, measuring air pollution, agricultural spraying, fish finding, oil pipeline inspection, monitoring of railways, monitoring of freeway traffic conditions, and monitoring of the seacoast, sea and mountain rescue, accident monitoring oil tankers, nuclear plants, firefighting in dangerous areas, volcanic eruptions, earthquakes, etc.

In particular, the four-rotor rotorcraft or quadrotor is appealing and superior from the control point of view. This type of rotorcraft attempts to achieve stable hovering, and low-speed flight by balancing the forces produced by the four rotors. One of the advantages of using a quadrotor is the increased pay-load capability because it has more lift than a conventional helicopter. It can be potentially used in some specific applications which demand stable hovering as well as low altitude flight such as aerial photography, low-speed surveillance, oil pipeline inspection and nuclear plant inspection (e.g. Fukushima Crisis, Japan) etc.

Recently, many intelligent control algorithms were developed for quad-rotor crafts. Abeywardena et al. proposed the fuzzy logic controller for stable hovering control of a quad-rotor craft [1]. Some model-based control schemes of quadrotor crafts have also been successfully developed [2] [3][4]. These control schemes unavoidably employed the inertial measurement units for orientation and positioning control; in addition to the inertial measurement, the GPS (Global Positioning System) receiver was usually incorporated to provide a long-period correction for positioning. They were mostly designed for moving in outdoor environments. If the quad-rotor craft is intended to be applied indoors, however, some alternative measurement system for positioning should be devised.

Only few papers in literature deal with the orientation and positioning control in indoor environment. In [6], visual systems are used for quad-rotor craft navigation, and in [7], vision-based guided method for the air-ground multi-robot system was proposed. This paper focuses on the problem of quad-rotor craft height estimation in the indoor environment. Visual servoing techniques [5][8] were employed for autonomous navigation and positioning. One of the main features is that only cameras are used as sensors for positioning and tracking control. The objective of this study is to develop an image tracking and height estimation scheme from the image sensing of a landmark.

Two multi-vision systems, namely, stereo vision system and humanoid vision systems, respectively, were employed for quad-rotor craft height estimation. An HVS (Hue-Saturation-Value) color based tracking algorithm was developed for image tracking of the landmark. The performances of the two vision systems were examined and compared. The experimental results demonstrate the effectiveness of both vision systems; nevertheless,

---

\*Corresponding Author: Juhng-Perng Su  
(E-mail: [sujp@mail.ndhu.edu.tw](mailto:sujp@mail.ndhu.edu.tw))

<sup>1</sup> Department of Electrical Engineering, National Dong Hwa University, No. 1, Sec. 2, Da Hsueh Rd., Shoufeng, Hualien, 97401, Taiwan, R.O.C.

<sup>2</sup> Department of Computer Science and Information Engineering, Far East University, Soochow University, No. 49, Chung-Hwa Road, Hsin-Shih, Tainan 74448, Taiwan, R.O.C.

the humanoid vision system looks better in accuracy of the height estimation of quad-rotor craft.

## 2. The Image Servoing System and Indoor Multi-rotor Craft

The block diagram of a Position-Based Visual Servo control (PBVS) system is depicted in Figure 1 where The motion vector of the target plays the key role. As can be seen

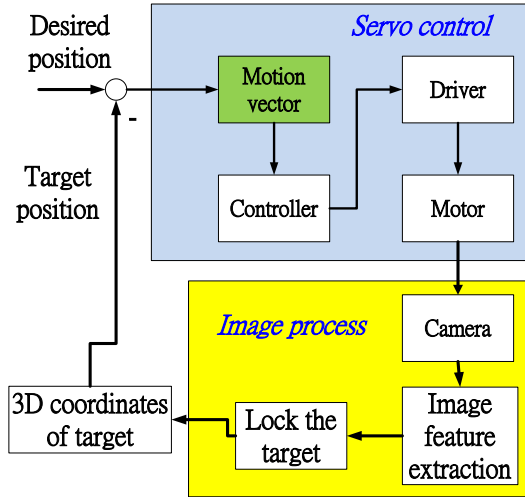


Figure 1: Position-based visual servo control (PBVS)

from Figure 2,

$$\theta = \tan^{-1} \left( \frac{V_y}{V_x} \right) \quad (1)$$

where  $V_x = X_{f(t)} - X_{f(t-1)}$ ,  $V_y = Y_{f(t)} - Y_{f(t-1)}$  and  $\tan^{-1}(\cdot)$  are the two-argument arctangent functions. Given

$$|V|^2 = V_x^2 + V_y^2 \quad (2)$$

the moving vectors along the pan and tilt directions are

$$\begin{cases} \text{Pan} = |V| * \cos \theta \\ \text{Tilt} = |V| * \sin \theta \end{cases} \quad (3)$$

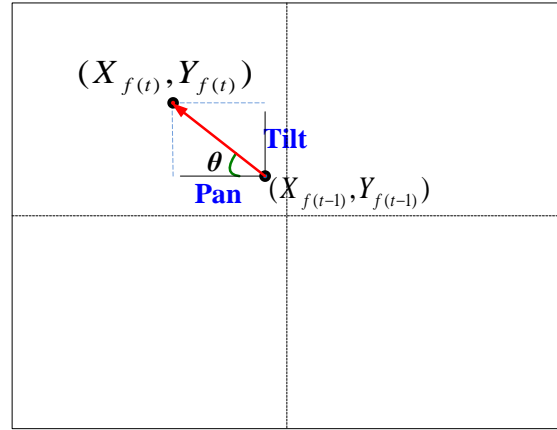


Figure 2: The motion vector computing

In this study, we employ the HSV color model, as illustrated in Figure 3, can be represented as a cone in a three-dimensional space.

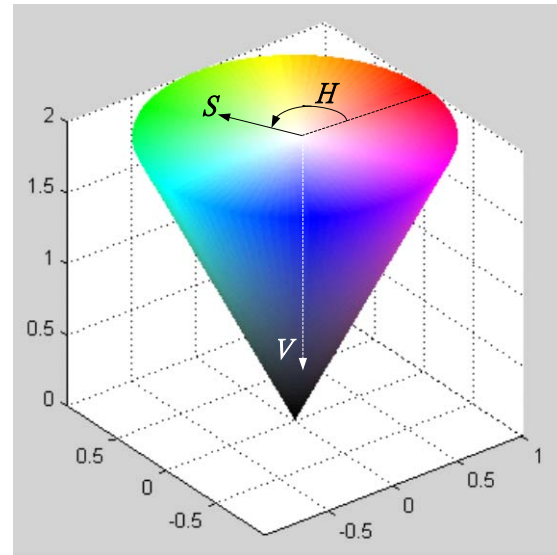


Figure 3: HSV color model

The RGB to HSV transformation is given as follows

$$\begin{aligned} V &= \max(R, G, B) \\ S &= \frac{(V - \min(R, G, B))}{V} \\ H &= \begin{cases} (G - B) * 60 / S, & \text{if } V = R \\ 180 + (B - R) * 60 / S, & \text{if } V = G \\ 240 + (R - G) * 60 / S, & \text{if } V = B \end{cases} \end{aligned} \quad (4)$$

Based on the HSV color model, the color features of target could be extracted easily.

A sketch of the quad-rotor craft in 3D space is illustrated in Figure 4, where a coordinate frame, called body frame, is attached for the description of its dynamics.

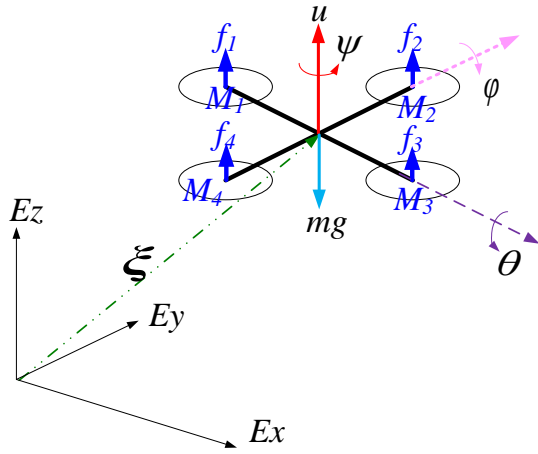


**Figure 4: Quad-rotor craft in 3D coordinate**

Usually, the fixed earth frame ( $E$ -frame), or called inertial frame, is used as a reference for observation. From Figure 4,  $f_1, \dots, f_4$  are the lift forces produced by motors  $M_1, \dots, M_4$  with motor speeds  $\Omega_1, \dots, \Omega_4$ . The magnitude of the lift force is proportional to the corresponding square of angular speed.

Let the position and the orientation of the quad-rotor craft are represented by the following vector:

$$\xi = [\mathfrak{I}^E \quad \mathfrak{R}^E]^T = [X \quad Y \quad Z \quad \varphi \quad \theta \quad \psi]^T, \quad (3)$$

where  $\mathfrak{I}^E$  and  $\mathfrak{R}^E$  represent, respectively, the position and orientation in Euler angles of the quad-rotor craft relative to the earth coordinate frame. The kinematics of a quad-rotor craft is the same as that of a 6-DOF rigid-body, which can be described as:

$$\dot{\xi} = \mathbf{J}_{\mathfrak{R}} \mathbf{v}, \quad (4)$$

$$\mathbf{v} = [\mathbf{V}^B \quad \boldsymbol{\omega}^B]^T = [u \quad v \quad w \quad p \quad q \quad r]^T, \quad (5)$$

where  $\mathbf{V}^B$  and  $\boldsymbol{\omega}^B$  are the linear and angular velocity of the body frame of quad-rotor craft, respectively.  $\mathbf{J}_{\mathfrak{R}}$  is the Jacobian matrix defined as follows:

$$\mathbf{J}_{\mathfrak{R}} = \begin{bmatrix} \mathbf{R}_{\mathfrak{R}} & \mathbf{0}_{3 \times 3} \\ \mathbf{0}_{3 \times 3} & \mathbf{T}_{\mathfrak{R}} \end{bmatrix}, \quad (6)$$

where  $\mathbf{R}_{\mathfrak{R}}$  is the rotation matrix and  $\mathbf{T}_{\mathfrak{R}}$  the translation matrix given, as follows

$$\mathbf{R}_{\mathfrak{R}} = \begin{pmatrix} \cos \phi \cos \theta & \cos \phi \sin \theta \sin \psi - \sin \phi \cos \psi & \cos \phi \sin \theta \cos \psi + \sin \phi \sin \psi \\ \sin \phi \cos \theta & \sin \phi \sin \theta \sin \psi + \cos \phi \cos \psi & \sin \phi \sin \theta \cos \psi - \cos \phi \sin \psi \\ -\sin \theta & \sin \psi \cos \theta & \cos \theta \cos \psi \end{pmatrix}, \quad (7)$$

$$\mathbf{T}_{\mathfrak{R}} = \begin{pmatrix} 1 & \sin \phi \tan \theta & \cos \phi \tan \theta \\ 0 & \cos \phi & -\sin \phi \\ 0 & \sin \phi / \cos \theta & \cos \phi / \cos \theta \end{pmatrix}. \quad (8)$$

The Newton-Euler dynamics of 6-DOF rigid-body [9] is

$$\begin{bmatrix} m\mathbf{I}_{3 \times 3} & \mathbf{0}_{3 \times 3} \\ \mathbf{0}_{3 \times 3} & \mathbf{I}_{ine} \end{bmatrix} \begin{bmatrix} \dot{\mathbf{V}}^B \\ \dot{\boldsymbol{\omega}}^B \end{bmatrix} + \begin{bmatrix} \boldsymbol{\omega}^B \times (m\mathbf{V}^B) \\ \boldsymbol{\omega}^B \times (\mathbf{I}\boldsymbol{\omega}^B) \end{bmatrix} = \begin{bmatrix} \mathbf{F}^B \\ \boldsymbol{\tau}^B \end{bmatrix}, \quad (9)$$

where  $\mathbf{I}_{ine}$  is the inertia matrix and  $m$  is the mass of the body.  $\dot{\mathbf{V}}^B$  and  $\dot{\boldsymbol{\omega}}^B$  are the linear and angular acceleration vectors of quad-rotor craft, respectively, expressed in body frame. Moreover, the  $\mathbf{F}^B$  and  $\boldsymbol{\tau}^B$  are the lift force and torque of the quad-rotor craft, respectively. Define the generalized force vector  $\boldsymbol{\varepsilon}$  as:

$$\boldsymbol{\varepsilon} = [\mathbf{F}^B \quad \boldsymbol{\tau}^B]^T = [F_x \quad F_y \quad F_z \quad \tau_x \quad \tau_y \quad \tau_z]^T. \quad (10)$$

Rewrite Eq. (10) in a matrix form [10] :

$$\mathbf{M}_I \dot{\mathbf{v}} + \mathbf{C}(\mathbf{v}) = \boldsymbol{\varepsilon}, \quad (11)$$

where  $\dot{\mathbf{v}}$  is the generalized acceleration vector,  $\mathbf{M}_I$  is the system inertia matrix, given as follows

$$\mathbf{M}_I = \begin{bmatrix} m\mathbf{I}_{3 \times 3} & \mathbf{0}_{3 \times 3} \\ \mathbf{0}_{3 \times 3} & \mathbf{I}_{ine} \end{bmatrix} = \begin{bmatrix} m & 0 & 0 & 0 & 0 & 0 \\ 0 & m & 0 & 0 & 0 & 0 \\ 0 & 0 & m & 0 & 0 & 0 \\ 0 & 0 & 0 & I_{XX} & 0 & 0 \\ 0 & 0 & 0 & 0 & I_{YY} & 0 \\ 0 & 0 & 0 & 0 & 0 & I_{ZZ} \end{bmatrix}. \quad (12)$$

Moreover,  $\mathbf{C}(\mathbf{v})$  is the Coriolis-centripetal matrix, given as follows

$$\mathbf{C}(\mathbf{v}) = \begin{bmatrix} \mathbf{0}_{3 \times 3} & -m\ell(\mathbf{V}^B) \\ \mathbf{0}_{3 \times 3} & -\ell(\mathbf{I}_{ine}\boldsymbol{\omega}^B) \end{bmatrix} = \begin{bmatrix} 0 & 0 & 0 & 0 & mw & -mv \\ 0 & 0 & 0 & -mw & 0 & mu \\ 0 & 0 & 0 & mv & -mu & 0 \\ 0 & 0 & 0 & 0 & I_{ZZ}r & -I_{YY}q \\ 0 & 0 & 0 & -I_{ZZ}r & 0 & I_{XX}p \\ 0 & 0 & 0 & I_{YY}q & -I_{XX}p & 0 \end{bmatrix}, \quad (13)$$

where  $\ell$  is the skew-symmetric operator.

In (11), the  $\varepsilon$  can be divided into three parts. They are gravity, the gyroscopic effects of rotors and the lift forces exerted on propeller axes, respectively. Accordingly, Eq. (11) can be further expressed in the following equations

$$\mathbf{M}_I \dot{\mathbf{v}} + \mathbf{C}(\mathbf{v}) = \mathbf{G}(\xi) + \mathbf{D}(\mathbf{v})\Omega + \mathbf{U}(\Omega), \quad (14)$$

$$\dot{\mathbf{v}} = \mathbf{M}_I^{-1}(-\mathbf{C}(\mathbf{v}) + \mathbf{G}(\xi) + \mathbf{D}(\mathbf{v})\Omega + \mathbf{U}(\Omega)), \quad (15)$$

where  $\mathbf{G}(\xi)$  is the gravity vector,

$$\mathbf{G}(\xi) = \begin{bmatrix} mg \sin \theta \\ -mg \cos \theta \sin \phi \\ -mg \cos \theta \cos \phi \\ 0 \\ 0 \\ 0 \end{bmatrix}, \quad (16)$$

and  $\mathbf{D}(\mathbf{v})\Omega$  is the gyroscopic effects of rotors,

$$\mathbf{D}(\mathbf{v})\Omega = \mathbf{J}_p \begin{bmatrix} 0 & 0 & 0 & 0 \\ 0 & 0 & 0 & 0 \\ 0 & 0 & 0 & 0 \\ q & -q & q & -q \\ -p & p & -p & p \\ 0 & 0 & 0 & 0 \end{bmatrix} \Omega. \quad (17)$$

In (17), the  $\mathbf{J}_p$  is the total rotational moment of inertia around the propeller axis and  $\Omega$  is the rotor speed vector

$$\Omega = [\Omega_1 \quad \Omega_2 \quad \Omega_3 \quad \Omega_4]^T \quad (18)$$

The external force vector  $\mathbf{U}(\Omega)$  exerted on the propeller axes is defined as:

$$\mathbf{U}(\Omega) = \begin{bmatrix} 0 \\ 0 \\ U_1 \\ U_2 \\ U_3 \\ U_4 \end{bmatrix} = \begin{bmatrix} 0 \\ 0 \\ b(\Omega_1^2 + \Omega_2^2 + \Omega_3^2 + \Omega_4^2) \\ bl(\Omega_4^2 - \Omega_2^2) \\ bl(\Omega_3^2 - \Omega_1^2) \\ d(\Omega_2^2 + \Omega_4^2 - \Omega_1^2 - \Omega_3^2) \end{bmatrix}, \quad (19)$$

where  $b$  and  $d$  are the thrust and drag coefficients, respectively and  $l$  is the length of the propeller axis from the rotor to the rotorcraft center of gravity.

For control purpose, it is preferable to express the equations of motion for quad-rotor craft in hybrid frame; specifically, the following generalized velocity vector is adopted

$$\delta = [\dot{\mathcal{X}}^E \quad \omega^B]^T = [\dot{X} \quad \dot{Y} \quad \dot{Z} \quad p \quad q \quad r]^T, \quad (20)$$

and the equation of motion can be expressed in the following form

$$\dot{\delta} = \mathbf{M}_H^{-1}(-\mathbf{C}_H(\delta)\delta + \mathbf{G}_H + \mathbf{D}_H(\delta)\Omega + \mathbf{U}_H(\delta)), \quad (21)$$

where

$$\mathbf{M}_H = \mathbf{M}_I, \quad \mathbf{D}_H(\delta)\Omega = \mathbf{D}(\mathbf{v})\Omega, \quad (22)$$

$$\mathbf{C}_H(\delta) = \begin{bmatrix} 0_{3 \times 3} & 0_{3 \times 3} \\ 0_{3 \times 3} & -\ell(I_{ine}\omega^B) \end{bmatrix}, \quad \mathbf{G}_H = \begin{bmatrix} 0 \\ 0 \\ -mg \\ 0 \\ 0 \\ 0 \end{bmatrix}, \quad (23)$$

$$\mathbf{U}_H(\delta) = \begin{bmatrix} (\cos \phi \sin \theta \cos \psi + \sin \phi \sin \psi)U_1 \\ (\cos \phi \sin \theta \sin \psi - \sin \phi \cos \psi)U_1 \\ (\cos \theta \cos \phi)U_1 \\ U_2 \\ U_3 \\ U_4 \end{bmatrix}. \quad (24)$$

Or, in a form of simultaneous nonlinear differential equations

$$\begin{cases} \ddot{X} = (\cos \phi \sin \theta \cos \psi + \sin \phi \sin \psi) \frac{U_1}{m} \\ \ddot{Y} = (\cos \phi \sin \theta \sin \psi - \sin \phi \cos \psi) \frac{U_1}{m} \\ \ddot{Z} = -g + (\cos \theta \cos \phi) \frac{U_1}{m} \\ \dot{p} = \frac{I_{YY} - I_{ZZ}}{I_{XX}} qr - \frac{\mathbf{J}_p}{I_{XX}} q\Omega + \frac{U_2}{I_{XX}} \\ \dot{q} = \frac{I_{ZZ} - I_{XX}}{I_{YY}} pr - \frac{\mathbf{J}_p}{I_{YY}} p\Omega + \frac{U_3}{I_{YY}} \\ \dot{r} = \frac{I_{XX} - I_{YY}}{I_{ZZ}} pq + \frac{U_4}{I_{XX}} \end{cases}. \quad (25)$$

### 3. Stereo Vision System

A 3D scenery projected to 2D image will lose the information of depth. The stereo vision approach is a commonly used method for measuring the depth. Consider a point  $Target=(X, Y, Z)$  in the 3D space captured by a stereo vision system, and the point P is projected on both left and right images. The geometric relationship is illustrated in Figure 5. In Figure 5, the projected coordinates of point P on the left and the right images are  $(x_l, y_l)$  and  $(x_r, y_r)$ , respectively.

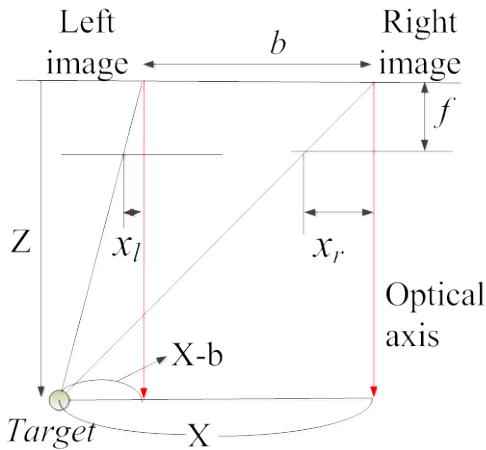


Figure 5: Geometric relationship of a stereo vision system

Based on triangulation, the formation of the left image is

$$\frac{X}{Z} = \frac{x_l}{f},$$

or

$$X = \frac{x_l}{f} Z \tag{26}$$

and the formation of the right image is

$$\frac{X-b}{Z} = \frac{x_r}{f} \tag{27}$$

From (26) and (27), we have

$$Z = \frac{fb}{(x_l - x_r)} = \frac{fb}{\Delta x} \tag{28}$$

where  $f$  is focal length,  $b$  is the length of baseline and  $\Delta x = (x_l - x_r)$  is the disparity. From (27), the accuracy of  $f$ ,  $b$  and  $\Delta x$  will influence the depth measuring. Specifically, the length of baseline is apparently an important parameter for stereo vision system design.

The stereo vision system composed of two webcams with resolutions of 0.3 mega pixels is shown in Figure 6. To simplify the system, we dismantled the cover of the webcams. The whole system is in fact very light in weight and thin in width.



Figure 6: The handmade stereo vision system

The stereo vision system involves “matching” and “3D reconstruction” processes. The disparity estimation which is considered the most important part of the stereo vision can be computed by the matching method. Accordingly, the 3D scene can be reconstructed based on the estimation of disparity. The phase-based image matching [11] is adopted here for our purpose. The images are firstly transformed into the frequency domain by 2D Discrete Fourier Transform (2D DFT) and, then, the best matching vector is derived by computing the phase correlation function.

### 4. Humanoid Vision System

The humanoid vision system is composed of two pan-tilt servo subsystems. The subsystem is shown in Figure 6 in which the two pan-tilt servo subsystems are used to drive the cameras to align the target at the same time. The geometric relationship between the respective target images via the two cameras is shown in Figure 6. Due to the special architecture of humanoid vision system, the complexity of the pair image matching problem and 3D coordinate computing problem [12] can be significantly simplified. For robot systems, this is quite preferable for real-time distance measuring application.



Figure 6: The humanoid vision system

As depicted in Figure 7 and Figure 8, the depth  $Z$  and height  $Q$  of an object can be obtained by the following equations,

$$\tan \alpha_1 = \frac{p}{Z}, \quad \tan \alpha_2 = \frac{D-p}{Z} \quad (29)$$

From (29), we have

$$Z \tan \alpha_1 = p \quad (30)$$

Substitutes (29) into (30) yields

$$\tan \alpha_2 = \frac{D - (Z \tan \alpha_1)}{Z} \quad (31)$$

The depth  $Z$  and the height  $Q$  can be obtained, respectively, as follows

$$Z = \frac{D}{(\tan \alpha_1 + \tan \alpha_2)} \quad (32)$$

$$Q = R \tan \alpha_3 \quad (33)$$

where  $R = [(D-p)^2 + Z^2]^{\frac{1}{2}}$ . The  $\alpha_1$ ,  $\alpha_2$  and  $\alpha_3$  are measured directly from the encoders of the pan-tilt servo systems.

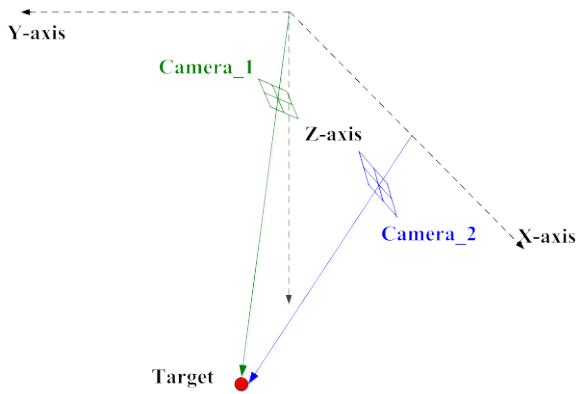


Figure 7: The geometric relationship of humanoid vision system

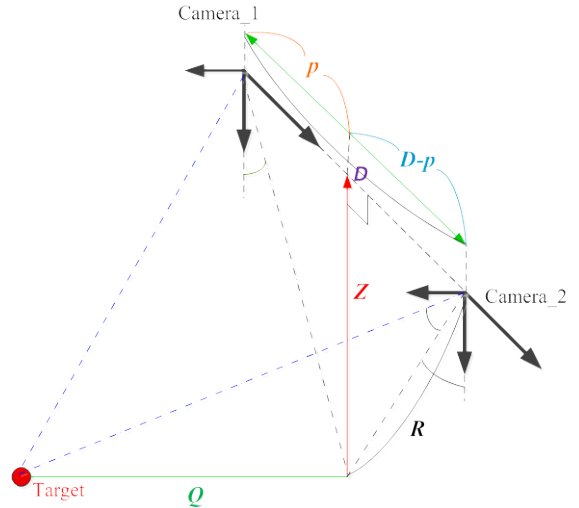


Figure 8: The target position estimation via humanoid vision

## 5. Experiment Results

There are three major parts in this section, the image segmenting, the performances of stereo vision system and humanoid vision system, and the height estimation results. The image segmentation results are illustrated in Figure 9. The left image is the real-time image, and the right image is the HSV color model segmenting result. In the indoor environment, the (10 cm radius) red target is used for the landmark. In Figure 9, the target is captured via color model segmenting result in every frame of video. The tracking results looks great. The quad-rotor craft is shown as Figure 10. The multi-vision systems are fixed at the bottom of quad-rotor craft.

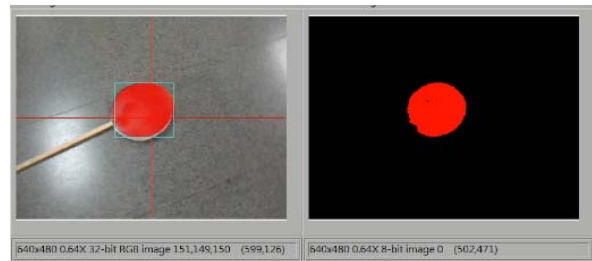
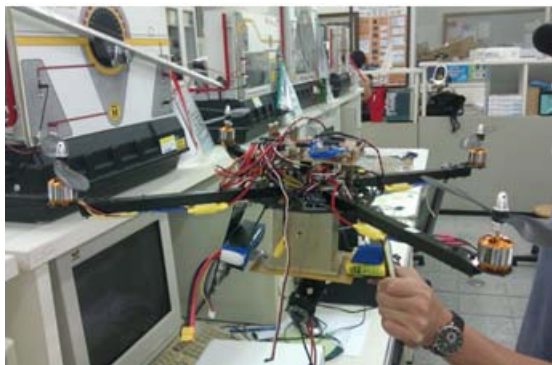


Figure 9: The segmenting and tracking results



**Figure 10: The quad-rotor craft with multi-vision system**

The stereo pairs are captured in the indoor environment by stereo vision and humanoid vision systems as illustrated in Figure 11 and Figure 12, respectively. In Figure 11, target is captured at height 1.65m. The baseline of the system is 15cm, and the error of height estimation is 0.07m. Likewise, in Figure 12 target is captured at height 1.95m. The baseline is 15cm, and the error of height estimation is 0.06m. Figure 13 and Figure 14 are the results of the stereo pairs in which targets are captured by humanoid vision and stereo vision systems in the outdoor environment, respectively.

Figure 13 indicates that the target is captured at height 3.9m. The baseline of the humanoid vision system is 15cm, and the error of height estimation is 0.29m. Likewise, in Figure 14 target is captured at height 3.5 m. The baseline of the stereo vision system is 15cm, and the error of height estimation is 0.41m. We summarize the estimating results of height from 0.5m to 4.5m in Figure 15.

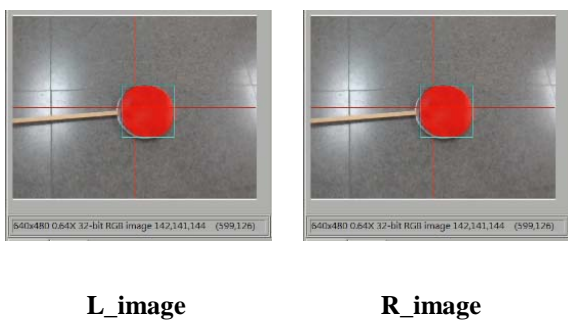


**Figure 11: Stereo vision system in indoor environment**

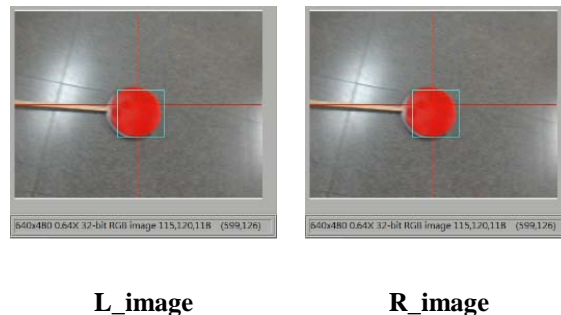


**Figure 12: Humanoid vision system in indoor environment**

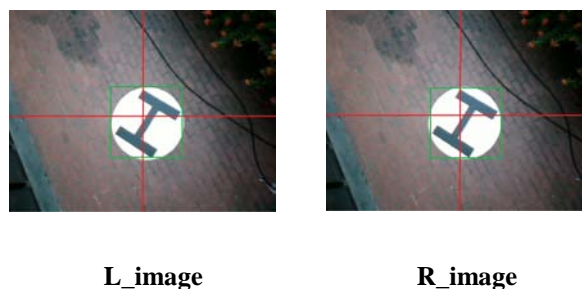


**Figure 13: Humanoid vision system in outdoor environment**

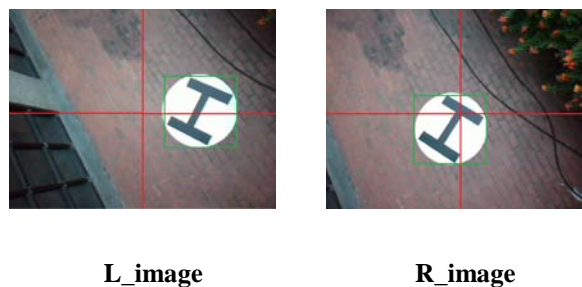


**Figure 14: Stereo vision system in outdoor environment**

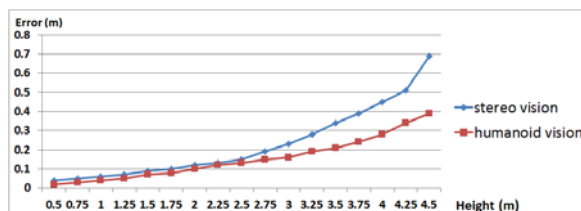


**Figure 15: Stereo vision system in indoor environment**

As can be seen from Figure 15, the estimation errors of stereo vision and humanoid vision system are almost the same under height 2.5 m; however, the estimation error of stereo vision increases remarkably when compared with humanoid vision system after height 2.5 m. At height 4.5 m, the estimation error of stereo vision reaches up to 70cm. On the other hand, the estimation error of humanoid vision is 40cm. The estimation error of humanoid vision system is only 57% of that of stereo vision at height 4.5m.

The actual flight test with image tracking is illustrated in Figure 16. In Figures 16- (a) and (b), targets are captured from the flight test video on the plane. The trajectory of the flight test video is recorded as in Figure 17.

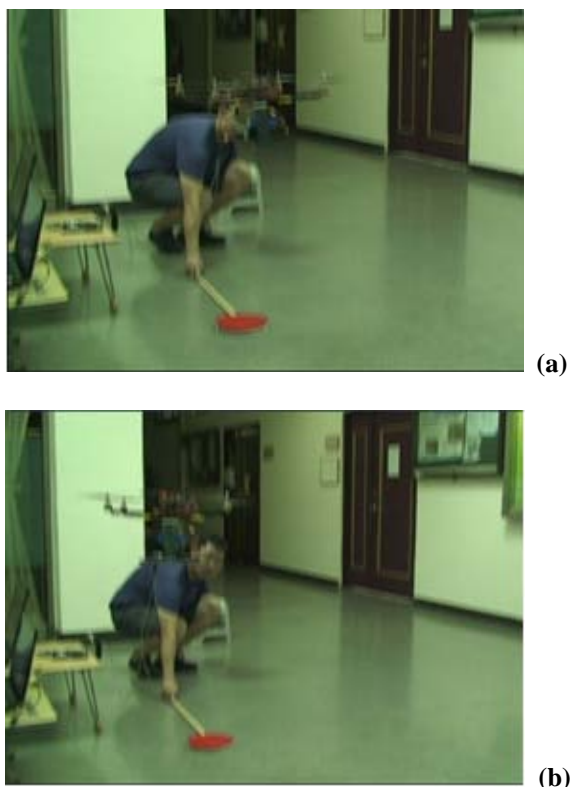


Figure 16. The actual flight test with image tracking

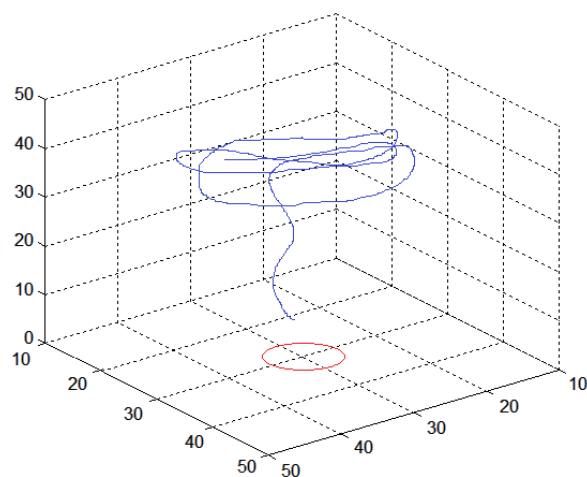


Figure 17 The trajectory of the flight test

## 6. Conclusions

In this paper, the image servoing techniques are used for height estimating and image tracking for indoor quad-rotor crafts from a landmark image. The height of the quad-rotor craft has been successfully estimated via both stereo vision system and humanoid vision. The HSV color model based tracking method is employed in this study for tracking the landmark image. The experimental results suggest that the target image can be effectively tracked via the proposed HSV color model based tracking method. We have devised a stereo vision system and a humanoid vision system implemented on a quad-rotor craft for the test of the corresponding performances of the estimation schemes. The accuracy of the quad-rotor height estimation via humanoid vision system looks better than that of the stereo vision system. The primitive results have paved a way for the future research on the design of a dexterous humanoid vision system for the study of quad-rotor SLAM (Simultaneous localization and mapping) problem.

## Acknowledgment

This study is supported in part by the National Science Council of the Republic of China under contract number NSC101-2221-E-259 -038.

## References

- [1] D. M. W. Abeywardena, L. A. K. Amaratunga, S. A. A. Shakoor, and S. R. Munasinghe, "A Velocity Feedback Fuzzy Logic Controller for Stable Hovering of a Quad Rotor UAV," in Proc., Interactional Conference on Industrial and Information Systems, Sri Lanka, 28 - 31 December, pp.558-562, 2009.
- [2] P. Pounds, R. Mahony, P. Hynes and J. Roberts, "Design of a Four Rotor Aerial Robot," in Proc., Australian Conference on Robot and Automation, Auckland, Australia, 27-29 November, pp. 145-150, 2002.
- [3] J. Wu, H. Peng, and Q. Chen, "RBF-ARX Model-based Modeling and Control of Quadrotor," in Proc., IEEE International Conference on Control Applications, Xiamen, China, 8-10 September, pp.1731-1736, 2010,
- [4] J. Li and Y. Li, "Dynamic Analysis and PID Control for a Quadrotor," in proc., 2011 IEEE International Conference on Mechatronics and Automation, Beijing, China, 7-10 August, pp. 573-578, 2011.
- [5] F. Chaumette, and S. Hutchinson, "Visual Servo Control Part1: Basic Approaches," IEEE Robotics and Automation Magazine, vol. 13, no. 4, pp. 82-90, 2006.
- [6] S. Ahrens et al., "Vision-Based Guidance and Control of a Hovering Vehicle in Unknown, GPS-denied Environments," IEEE International Conference on Robotics and Automation, Kobe, Japan, 12-17 May, pp. 2643-2648, 2009.
- [7] W. Li, T. Zhang, K. Kuhnlenz, "A Vision-Guided Autonomous Quadrotor in An Air-Ground Multi-Robot System," in Proc., IEEE International Conference on Robotics and Automation, 9-13May, Shanghai, China, pp. 2980-2985, 2011.
- [8] S. A. Hutchinson, G. D. Hager, and P. I. Corke, "A Tutorial on Visual Servo Control," IEEE Transaction on Robotics and Automation, vol. 12, no. 5, pp.651- 670, 1996.
- [9] T. Bresciani, Modeling, Identification and Control of a Quadrotor Helicopter, Department of Automatic Control, Lund University, 2008.
- [10] T. Perez, Ship Motion Control: Course Keeping and Roll Stabilization using Rudder and Fins, Springer, New York, 2005.
- [11] M. A. Muquit, T. Shibahara and T. Aoki, "A High-Accuracy Passive 3D Measurement System Using Phase-Based Image Matching," IEICE Transactions on Fundamentals of Electronics, Communications and Computer Sciences, vol. E39-A, no. 3, pp. 686-697, 2006.
- [12] K. H. Hsia, S. F. Lien, J. P. Su, "Camera position estimation and feature extraction from an incomplete image of a landmark", Artif Life Robotics, Vol 16, pp.152-156, 2011.



Juhng-Perng Su: He received the Ph.D. degree in electrical engineering from Sun Yat-Sen University, Kaohsiung, Taiwan, in 1990. From 1991 to 2012, he was with the Department of Electrical Engineering, National Yunlin University of Science and Technology. He is currently a professor of the Department of Electrical Engineering, National Dong-Hwa University, Hualien, Taiwan. Since 2004, Dr. Su has been conducting research projects granted from NSC on autonomous unmanned helicopters and has published some papers on this topic. Dr. Su was a recipient of the distinguished research award from Yunlin University of Science and Technology in 2005. His current research interests include the design of autonomous unmanned rotorcrafts, robust estimation and optimal control, intelligent robots and controller realization with embedded MCUs.



Kuo-Hsien Hsia: He received the Ph.D. degree in electrical engineering from National Sun Yat-Sen University, Ksohsiung, Taiwan, in 1994. He is currently an associate professor of the Department of Computer Science and Information Engineering, Far-East University, Taiwan. His research interests are in the area of differential game theory, fuzzy theory, image-assistant measurement and control software design.